



OPEN

DATA DESCRIPTOR

LiDAR-based topographic data for the coastline of Port Foster (Deception Island, Antarctica)

Alejandro Román¹✉, Antonio Tovar-Sánchez¹, Marcos Larrad², Federico Alva³ & Gabriel Navarro¹

The need to gather data in such a harsh, isolated, and hard-to-access environment as Antarctica is a priority for the scientific community aiming to understand this system's responses to different climate change scenarios. FosterCoast is a dataset collected using a UAV-based LiDAR sensor during the Spanish Antarctic Campaign 2024–2025 (Austral summer 2025), covering the entire inner ring (~35 km) of Port Foster Bay on Deception Island (Antarctica). It comprises the original data along with topographic products – such as orthomosaics, DEMs, and point clouds – derived from the photogrammetric processing of 13 UAV surveys, which include a total of 5,631 high-resolution RGB captures with Post-Processing Kinematic positioning. FosterCoast, available for public download via the Figshare data repository, represents the first complete UAV-based survey covering the entire Port Foster Bay within the volcanic ecosystem of Deception Island. This highly detailed dataset is a valuable asset for the polar scientific community, as well as for other relevant sectors, including the rescue operations, tourism, and navigation.

Background & Summary

Antarctica is among the Earth's regions experiencing the fastest and most diverse impacts of climate change^{1,2}. Specifically, changes in the vast and dynamic Antarctic coastal periphery have been driven by rising sea surface temperatures³ and cryogenic phenomena such as the decline of sea ice and permafrost^{4,5}, both of which have played a decisive role in coastal dynamics, directly impacting the structure of ecological communities^{6,7}, coastal erosion and geomorphology^{8,9}, and the ecosystem services they provide. Consequently, there is a compelling need for consistent and ongoing monitoring of the Antarctic coastline across space and time to reliably anticipate its potential responses to the changing climate and the effects of coastal transformation¹⁰.

Particularly, Port Foster Bay on Deception Island (South Shetland Islands, Antarctica) is of scientific interest because all these changes in the coastline, driven by the aforementioned processes, are also influenced by its incipient volcanic activity^{11–14}. In addition, the island's increasing human activity^{15–17}, as well as the presence of Antarctic research stations¹⁸, highlight the need to understand the geomorphology of the coastline in Port Foster to ensure safe evacuation routes and mobility pathways that can adapt to new and unexpected volcanic and glacial events¹⁹. However, most global studies analysing coastline changes to assess the contributions of glacier ice mass and ice sheets to sea-level rise in Antarctica do not consider Deception Island's contributions relevant due to its limited coverage compared to larger regions^{20,21}, so specific studies need to be developed. In fact, it has historically been challenging to accurately assess changes in the coastline of Port Foster Bay's inner ring, due to the limited number of scientific studies available^{22,23}, and the use of varying scales, geodetic datums, and map projections in existing cartographic materials¹⁹. The most recent approach has been presented by Torrecillas *et al.*¹⁹, which compiles the available data on Deception Island's coastline evolution, obtained through orthophotos, satellite images, and cartographic information from 1968 to 2020. However, this database is limited due to the island's almost permanent cloud cover, which affects satellite and aerial remote sensing, and it has low spatial resolution to monitor some of the most relevant coastal features for the scientific community, navigation, and tourism activities in general^{24,25}.

¹Institute of Marine Sciences of Andalusia (ICMAN), Spanish National Research Council (CSIC), Department of Ecology and Coastal Management, 11510, Puerto Real, Spain. ²Spanish Hydrographic Office (IHM), Spanish Army, Ministry of Defense, 11007, Cádiz, Spain. ³ATyges Engineering, 29590, Málaga, Spain. ✉e-mail: a.roman@csic.es

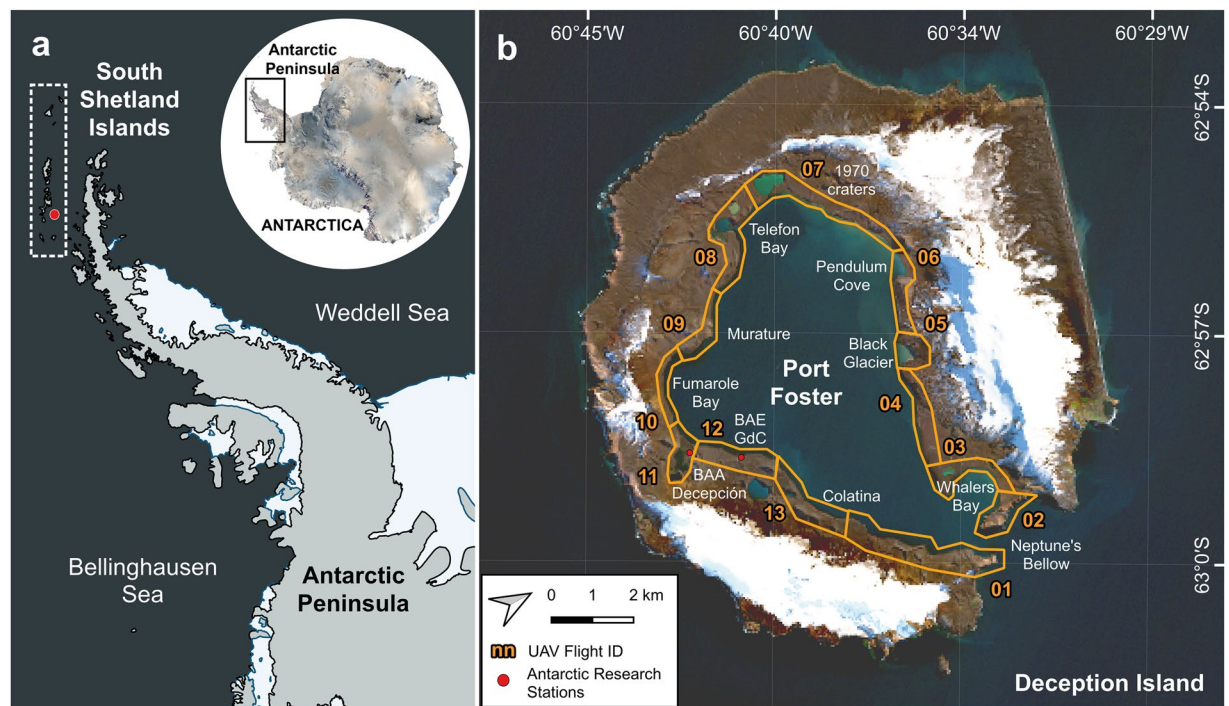


Fig. 1 Map illustrating: (a) a general overview of Antarctica highlighting the Antarctic Peninsula and the South Shetland Islands, created using the QAntarctica package (QAntarctica⁵⁰); (b) Sentinel 2A scene of Deception Island on March 17th, 2023, displaying the route followed by the UAV in each of the flights surveyed for data collection.

Here, we present FosterCoast, a dataset aimed at reducing the existing uncertainty in accurately extracting the coastline of Port Foster Bay on Deception Island (South Shetland Islands, Antarctica), leveraging the centimeter-level spatial resolution provided by Unmanned Aerial Vehicle (UAV)-based LiDAR technology. In this regard, it comprises both high-resolution LiDAR and photogrammetric products, as well as the original raw data, obtained from 13 UAV flights at multiple locations of interest within the inner ring of the bay, monitored during the Spanish Antarctic Campaign 2024–2025. The Pix4D Mapper (Pix4D SA, Lausanne, Switzerland, v.4.8.3) and DJI Terra (DJI, Da-Jiang Innovations, Shenzhen, China, v.4.3.0) software were used to process the collected data, following a workflow in which a Post Processing Kinematic (PPK) technology process was applied to ensure georeferencing accuracy. To our knowledge, this repository constitutes the first comprehensive UAV-based survey of the entire Port Foster Bay, offering a valuable resource for both the polar scientific community and other involved sectors (*e.g.* rescue operations, navigation, etc). Indeed, it would be useful for supporting: (i) the development of nautical charts, providing an accurate approximation of the coastline; (ii) the analysis of geomorphological changes in the coastline to determine whether erosion or accretion has occurred due to sediment transport and other factors; (iii) coastal habitat mapping through LiDAR and RGB optical technology; (iv) the elaboration of contour lines and the study of volcanic caldera evolution through updates to existing Digital Elevation Models (DEMs); (v) ongoing projects and time series conducted by other scientific institutions on the island; and (vi) hydrography studies and cryogenic process analysis related to the glaciers of Port Foster Bay.

Methods

Sites description. Deception Island (South Shetland Islands, Antarctica), located between latitudes 62°53'S and 63°01'S and longitudes 60°29'W and 60°45'W, is the youngest (probably less than 5 million years old) and most geologically active volcano along the Bransfield Strait's spreading center^{15,26}, with over 20 recorded eruptions in the past 200 years. The island's current geomorphology is defined by a major eruption that led to the collapse of its main volcanic edifice, resulting in the formation of the horseshoe-shaped, sea-flooded caldera known as Port Foster, which opens to the ocean via the narrow passage called Neptune's Bellows^{27,28}. Since then, post-caldera volcanic activity, along with glacial processes and the presence of permafrost, has shaped the island's landscape, thus featuring nearly 60 well-preserved craters (*e.g.* Soto crater, Chacao crater, Crater Lake, or 1970 craters), as well as streams, lakes, diverse landforms and deposits. The island also contains consolidated andesitic lapilli tuffs, such as the Murature formation¹, along with glaciers, partly ice-cored moraines, and glacial ice overlain by pyroclastic deposits, such as those found at Black Glacier, Red Glacier, and Green Glacier^{23,27}.

Almost the entire inner ring of Port Foster is the focal point of the island's geothermal activity, characterized by fumarolic emissions and areas of heated ground along the coastline in regions such as Fumarole Bay, Pendulum Cove, Telefon Bay, and Whalers Bay, where ground temperatures typically range from 40 to 60 °C, with some spots exceeding 110 °C²⁹. As a result, this geothermal activity has become one of the island's main

tourist attractions, drawing approximately 30,000 visitors per year since 1966 and making Deception Island one of the most popular tourist destinations in Antarctica (IAATO, International Association of Antarctica Tour Operators). However, the island was first discovered in 1820, and since then, it has been actively used for commercial exploitation of the Southern Ocean and, specifically, Whalers Bay served as a key shore base for Antarctica's major whaling industry between 1905 and 1930¹⁵. In addition, due to its strategic location and scientific importance, Deception Island hosts the Argentine (Decepción) and Spanish (Gabriel de Castilla, BAE GdC) research stations, which have operated every Antarctic summer since 1989, though not continuously throughout history¹⁵.

In terms of biodiversity, the island is home to exceptionally rare and diverse bryophyte communities that thrive in soil crusts heated by geothermal activity^{1,30}. However, these communities are not particularly abundant and are dispersed across various locations on the island, many of which are designated as Antarctic Specially Protected Areas (ASPA), such as Hot Hill (where temperatures reach up to 100 °C in some spots) and the previously mentioned Whalers Bay. On the other hand, the island's rugged and sheltered morphology, particularly within its inner ring, along with easy access to some volcanic sand and rock beaches, has allowed the establishment of penguin colonies, such as the chinstrap penguins (*Pygoscelis antarcticus*) at Entrance Point, as well as sea lion colonies, including one located between Neptune's Bellows and Collins Point.

This research focuses its area of action on Port Foster Bay, which was fully surveyed between January 29th and February 3rd, 2025, using UAV-based LiDAR and optical RGB imagery, with a focus on some of the aforementioned locations of interest (Fig. 1, Supplementary Figure 1).

UAV equipment and sensors. The data in this repository were collected using the DJI Matrice 300 RTK (M300) quadcopter equipped with the DJI Zenmuse L2 sensor. This UAV, weighing 9 kg at take-off, has a flight autonomy of around 35 minutes when carrying sensors, though this can vary with weather conditions. Moreover, its capability to withstand strong winds up to 15 m/s and operate in temperatures ranging from −20 to 40 °C makes it well-suited for Antarctica's harsh environment. The DJI Zenmuse L2 LiDAR sensor operates with a 240 Hz laser pulse, which supports up to five returns, and has a detection range of 2 cm to 450 m with 50% reflectivity and 0 klx. It also features a high-precision 200 Hz IMU and a 20 MP 4/3 CMOS camera that captures RGB images using a mechanical shutter speed from 2 to 1/2000 seconds and an electronic shutter speed from 2 to 1/8000 seconds, all stabilized by a 3-axis gimbal. According to manufacturer testing under controlled conditions, the sensor achieves vertical accuracy of 5 cm and horizontal accuracy of 10 cm for the RGB camera, with the IMU providing roll and pitch accuracy of 0.025° and yaw accuracy of 0.15°.

UAV data collection. All UAV operations in this study complied with Spanish Civil Aviation regulations set by the Spanish Aviation Safety Agency (AESA) and adhered to environmental protocols recommended by the Scientific Committee on Antarctic Research (SCAR)³¹ to minimize ecological impact. In addition, the recommendations of Hodgson & Koh³² were followed when operations involved wildlife, and all observations were recorded to build an evidence base for refined guidelines applicable to future research. Flight planning was carried out using the DJI Pilot application (DJI, Da-Jiang Innovations, Shenzhen, China, v.05.02.13.02), integrated into the UAV controller. This software enables automated aircraft operation and data collection according to a set of pre-established parameters (e.g. flight altitude above sea level, speed, duration, trajectory, capture overlap, among others). Furthermore, the software accounted for the terrain's topographic features, although surface morphology variations generally resulted in slight changes in Ground Sampling Distance (GSD) for each capture, so that the final GSD value was obtained as the average of all captures. All operations, as well as the parameters used in flight planning, are summarised in Table 1. Ground Control Points (GCPs) were not used for positioning, as many of the study areas were either too remote to access easily or large enough to be fully covered without them. Instead, Post-Processing Kinematic (PPK) georeferencing was performed using the DJI Zenmuse L2 sensor, in combination with a Reach RS2 + RTK GNSS antenna (EMLID) and the GNSS station located at the BAE GdC as reference stations (GNSS Service Spanish Geographic Institute [IGN])³³. By manually inputting precise known-point coordinates, the system calculated positioning errors and applied corrections, allowing for centimeter-level accuracy even without real-time correction capabilities.

LiDAR and Photogrammetric processing. The raw LiDAR data were processed using DJI Terra software (version 4.3.0, Da-Jiang Innovations, Shenzhen, China) to produce georeferenced, true-colour topographic outputs, including a 3D point cloud and a Digital Elevation Model (DEM). After importing all UAV images and positioning metadata, a point cloud in LAS format was generated with a spacing of 20 cm and an effective range of 40 to 200 m. From this point cloud, a DEM at a 1:500 scale was created. As mentioned earlier, the positioning of each point cloud was corrected using a PPK process, in which the central point of the base station served as a reference to provide accurate coordinates to the final product.

For the photogrammetric processing, the workflow outlined by Román *et al.*³⁴ was followed. Pix4D Mapper software (version 4.8.3, Pix4D SA, Lausanne, Switzerland) was employed to compile all image captures from each UAV flight into a single, georeferenced optical RGB orthomosaic. This software, whose performance has been extensively evaluated for generating topographic products^{35–37}, is capable of producing centimeter-level resolution orthomosaics using a Structure from Motion (SfM) photogrammetry process. The data processing workflow in Pix4D Mapper follows three well-defined steps: (i) “Image alignment”, where keypoints are identified using full-image scale (approximately half the original image size), and images are matched via triangulation with a maximum of five image pairs per Manual Tie Point (MTP). Internal and external camera parameters are then automatically optimized using a standard calibration model. (ii) A “3D dense cloud” is generated from the aligned images, using half-resolution input with optimized point density and requiring at least three matching

ID	Covered Locations	Key aspects	Central Coordinates	Date	Average GSD (cm/px)	# Images	Flight Time	Weather Conditions	LiDAR Overlapping	Covered Area (ha)
01	Entrance Point, Collins Point, Colatina	Sea lion and penguin colonies, and a stretch of rocky and icy coastline	62°59'05"S 60°40'05"W	Feb 3 rd , 2025	4.56	489	45 min	Cloudy	70% frontal 50% lateral	166.3407
02	Fildes Point at Neptune's Bellow, The Chilean's Window	Cliffs	62°59'14"S 60°33' 02"W	Jan 29 th , 2025	6.50	145	16 min	Partly cloudy	70% frontal 50% lateral	93.1124
03	Whalers Bay, Kroner Lake, Ronald Hill	Thermal anomalies and anthropic impacts	62°59'04"S 60°33'35"W	Jan 29 th , 2025	4.82	390	28 min	Partly cloudy	70% frontal 50% lateral	150.9432
04	Green Glacier, Red Glacier	Glacier	62°58'05"S 60°35'16"W	Jan 29 th , 2025	4.70	317	37 min	Partly cloudy	70% frontal 50% lateral	142.7793
05	Black Glacier, Good Weather Point	Glacier	62°57'15"S 60°35'30"W	Feb 4 th , 2025	4.07	1489	96 min	Cloudy and snowy	70% frontal 50% lateral	112.3725
05bis	Black Glacier, Good Weather Point	Glacier	62°57'15"S 60°35'30"W	Jan 29 th , 2025	4.25	399	52 min	Cloudy and snowy	70% frontal 50% lateral	174.7294
06	Pendulum Cove, Crimson Hill	Thermal anomalies	62°55'38"S 60°36'57"W	Jan 29 th , 2025	4.70	302	31 min	Partly cloudy and snowy	70% frontal 50% lateral	160.9990
07	1970 Craters, Hidden Lake	Periglacial lakes in a volcanic caldera	62°55'00"S 60°39'29"W	Jan 29 th , 2025	4.75	371	55 min	Partly cloudy and snowy	70% frontal 50% lateral	164.5883
08	Telefon Bay, Chacao Crater, Cross Hill	Inner bay with some periglacial lakes in volcanic craters	62°55'37"S 60°40'56"W	Jan 30 th , 2025	4.89	327	32 min	Partly cloudy and windy	70% frontal 50% lateral	167.9738
09	Murature, Obsidian Bay	Consolidated andesitic lapilli tuff	62°57'56"S 60°42'56"W	Jan 30 th , 2025	4.79	290	23 min	Partly cloudy and windy	70% frontal 50% lateral	92.7545
10	Fumarole Bay	Thermal anomalies	62°58'21"S 60°42'27"W	Jan 30 th , 2025	4.94	328	25 min	Partly cloudy and windy	70% frontal 50% lateral	184.8793
11	Hot Hill, Argentine Base Deception	Thermal anomalies and Argentine Antarctic Station	62°58'36"S 60°42'14"W	Feb 3 rd , 2025	4.36	168	19 min	Cloudy	70% frontal 50% lateral	49.0879
12	BAE GdC	Spanish antarctic station	62°58'37"S 60°40'31"W	Jan 29 th , 2025	4.78	339	36 min	Partly cloudy	70% frontal 50% lateral	146.9674
13	Soto Crater, Colatina	Periglacial lakes in a volcanic caldera and a stretch of rocky and icy coastline	62°58'41"S 60°40'29"W	Jan 30 th , 2025	4.51	346	41 min	Partly cloudy and windy	70% frontal 50% lateral	151.5148

Table 1. Details on UAV operations and flight conditions at each survey site along the coastal fringe of Port Foster at Deception Island (South Shetland islands, Antarctica). BAE GdC: Spanish Antarctic Base “Gabriel de Castilla”; GSD: Ground Sampling Distance.

points per feature. The point cloud is then filtered to visually remove outliers in poorly resolved areas (e.g. points located at anomalous elevations corresponding to water, snow, or fog below the flight altitude), and a 3D textured mesh is then created using a maximum Octree depth of 14 and limiting decimation to 5000 triangles. (iii) Finally, an interpolated Digital Surface Model (DSM) is derived from the 3D dense cloud and subsequently used as a reference for rendering the final orthomosaic.

All topographic outputs in this dataset are georeferenced using the WGS84/UTM Zone 20S coordinate system (EPSG: 32720).

Data Records

The FosterCoast dataset, which is divided into multiple ZIP files based on study locations previously listed in Table 1, is publicly available and easily downloadable from the Figshare repository³⁸. The ZIP files are divided into two categories for each flight ID, according to Table 1: (i) *RAW_ID*, including the original RAW data; and (ii) *Topo_ID*, including the topographic products (LiDAR point clouds, DEMs, and RGB orthomosaics) generated from the processing of each UAV flight on the corresponding dates. Each *Topo_ID* folder contains subfolders with, on one hand, the captures processed in PPK for the generation of orthomosaics (*PPK processed folder*), and on the other hand, the original captures with positioning files for LiDAR processing (*LiDAR processing folder*). Within each ID subfolder in the *Topo_ID* folder, the generated DEMs and RGB orthomosaics are stored in GeoTIFF (.tif) format, while LiDAR point clouds are provided in LAS (.las) format. Each final product file is named following this format: *YYYYMMDD_ID_PRO_L2*; where *YYYYMMDD* represents the flight date (*YYYY* for year, *MM* for month, and *DD* for day); *ID* corresponds to the number assigned to each study location in Table 1 (ranging from 1 to 13); *PRO* indicates the topographic product (*OR* for the RGB orthomosaic, *DEM* for the Digital Elevation Model, *PC* for the point cloud, and *RP* for the accuracy reports); and finally, *L2* refers to the sensor used to collect data, which in this case is always the DJI Zenmuse L2.

Accompanying each processed topographic product are detailed accuracy reports, which are automatically generated during RAW data processing using both DJI Terra and Pix4D Mapper software. On one hand, the

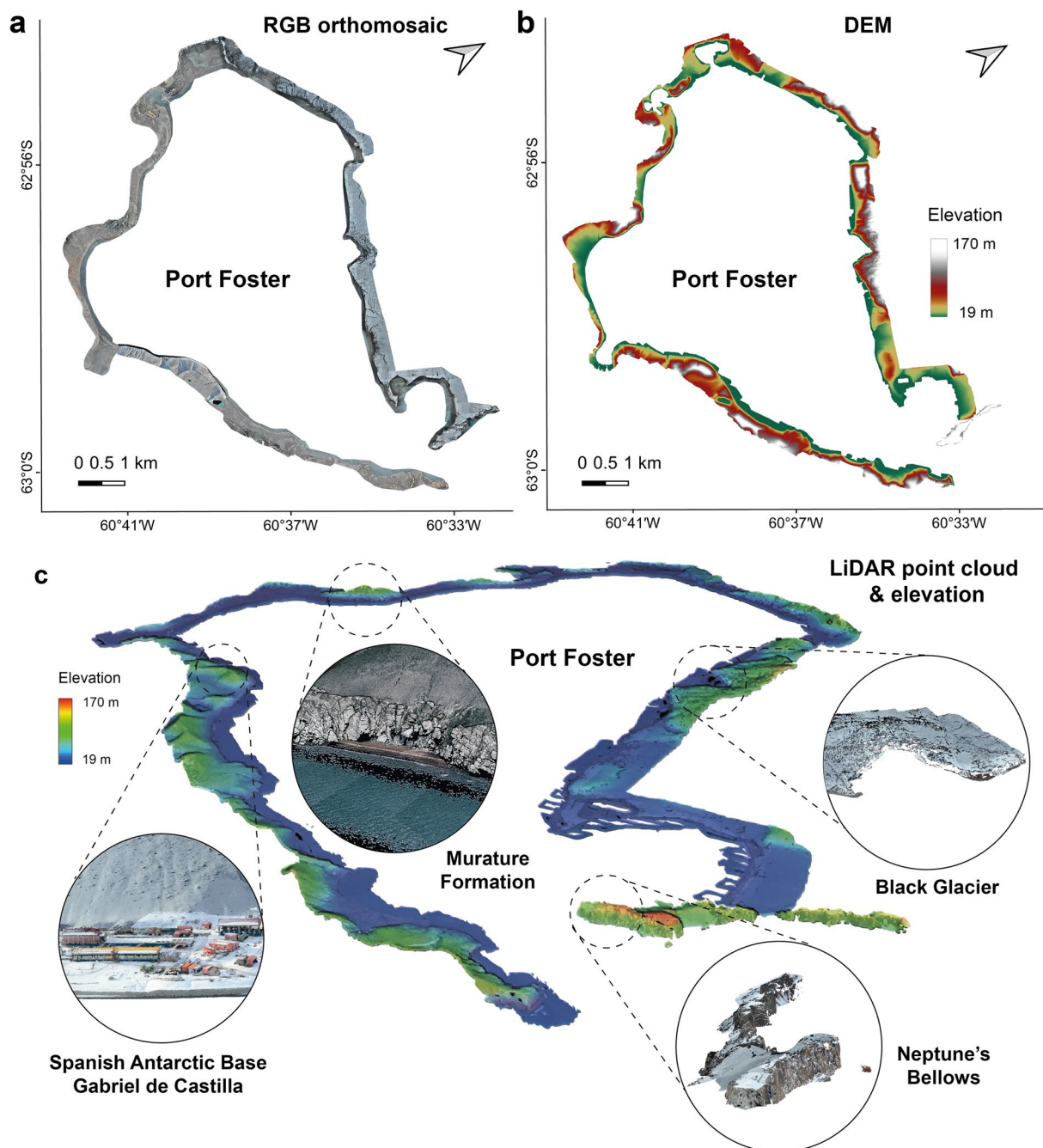


Fig. 2 Maps showing the entire inner ring of Port Foster on Deception Island (South Shetland Islands, Antarctica), including: (a) RGB orthomosaic; (b) DEM; (c) LiDAR point cloud with superimposed elevations, with detailed zooms on specific locations of interest.

DJI Terra report includes the following: (i) the parameters selected for the reconstruction and generation of topographic products; (ii) aircraft parameters, including LiDAR and IMU calibration periods during the flight; (iii) positioning accuracy parameters and IMU trajectory error details; (iv) a preview of the generated DEM; and (v) information on point cloud density. On the other hand, the Pix4D Mapper report, in addition to providing a summary highlighting key characteristics of the final products (including the optical RGB orthomosaic), includes the following: (i) a preview of the photogrammetric products generated after data processing; (ii) camera calibration data encompassing initial image positions, computed tie point locations, areas of image overlap, and absolute uncertainty values linked to the sensor's positioning and orientation; (iii) a summary of bundle block adjustment results and an assessment of geolocation precision; and (iv) a comprehensive description of the parameters selected at each processing step to ensure data processing reproducibility. Additional guidance for interpreting the accuracy assessment reports is included in the “Technical Validation” section, while a general visual summary of all surveyed locations is provided in Fig. 2.

Product ID	Camera Optimization (%)	Mean Reprojection Error (pixel)	Geolocation RMSE Error (cm)			IMU Trajectory Error					
			x	y	z	X(E) RMSE (cm)	X(E) Average (cm)	Y(N) RMSE (cm)	Y(N) Average (cm)	Z(U) RMSE (cm)	Z(U) Average (cm)
20250203_01	3.080	0.173	0.716	0.952	2.447	0.010	0.641	0.007	0.513	0.008	0.663
20250129_02	3.060	0.163	21.120	26.525	51.372	0.010	0.641	0.007	0.513	0.007	0.663
20250129_03	2.880	0.182	0.505	0.691	1.304	0.009	0.641	0.006	0.513	0.007	0.663
20250129_04	3.250	0.172	0.358	0.315	0.938	0.014	0.646	0.009	0.514	0.012	0.666
20250204_05	3.050	0.128	2.494	3.217	1.269	0.012	0.644	0.008	0.513	0.010	0.665
20250129_05bis	3.120	0.165	0.456	0.558	0.858	0.013	0.644	0.008	0.513	0.010	0.665
20250129_06	2.950	0.173	0.356	0.263	0.716	0.009	0.640	0.007	0.512	0.007	0.663
20250129_07	3.150	0.173	0.484	0.547	0.823	0.010	0.642	0.007	0.514	0.009	0.664
20250130_08	3.110	0.178	0.821	0.800	1.184	0.012	0.645	0.009	0.515	0.011	0.666
20250130_09	3.100	0.175	1.028	0.607	1.027	0.010	0.643	0.006	0.512	0.007	0.663
20250130_10	3.390	0.173	0.967	0.726	1.019	0.010	0.643	0.006	0.512	0.006	0.663
20250203_11	3.110	0.169	2.278	9.870	1.571	0.012	0.644	0.008	0.516	0.011	0.665
20250129_12	3.090	0.187	0.351	0.339	1.359	0.010	0.642	0.007	0.514	0.009	0.664
20250130_13	3.130	0.168	0.613	0.702	1.299	0.010	0.642	0.007	0.513	0.008	0.664

Table 2. Overview of key relative accuracy metrics for each processed UAV flight.

Technical Validation

According to the technical validation conducted by Román *et al.*³⁴, the quality of the generated topographic products has been assessed based on the geolocation, overlapping, and reprojection accuracy reported in the automatically generated reports from both processing software, Pix4D and DJI Terra. Table 2 provides a summary of the key relative accuracy metrics obtained during the processing of each UAV survey.

The intercomparison of topographic products generated from UAV-collected data, as well as their applications, requires highly accurate geolocation. Generally, the only truly reliable way to obtain precise positioning data for a UAV survey is by deploying Ground Control Points (GCPs) on the terrain. However, in vast, difficult-to-reach regions with extreme conditions such as Antarctica, the GCP-based georeferencing method presents a major limitation due to safety and logistical constraints³⁹. Although we continuously collected positional data using a Reach RS2 + RTK GNSS antenna, Real-Time Kinematic (RTK) positioning requires a stable radio link between the antenna and the UAV^{40,41} – an immense challenge in such a remote region where internet connectivity is limited. Consequently, in this study, the positioning error of all UAV surveys has been significantly reduced post-flight through a PPK geotagging process using RINEX GNSS positioning files provided by the Spanish Geographic Institute (IGN). This approach eliminates the risk of data loss due to link outages, as could occur with the RTK system, since all information is processed afterward, thus mitigating the need to apply GCPs⁴². According to the geolocation RMSE statistics, values below 0.05 m were achieved for all axes in all UAV operations, except for flight 20250129_02, where significant height differences influenced the resulting error – though it remained non-significant. Moreover, the Inertial Measurement Unit (IMU) trajectory error, which refers to the deviation of the drone's trajectory from the true motion path, is reported to be consistently up to ~ 0.005 m in the worst-case scenario. This indicates excellent accuracy in LiDAR data processing, as trajectory errors are well controlled, ensuring that point clouds remain precise with minimal distortions, making them suitable for high-precision applications such as those described in the Usage Notes section.

Regarding the quality of the overlap for generating topographic products (*i.e.* orthomosaics, DEMs, and point clouds), the reports from both software provide a graphical representation indicating the number of scenes overlapping for a specific pixel or a given number of pixels. When working with such fine spatial resolutions, a pixel in the generated products is considered accurate when it is integrated by at least five different scenes^{43,44}. However, even when the overlap in certain areas is adequate, the presence of homogeneous regions (*e.g.* water or snow surfaces) or adverse weather conditions (*e.g.* fog, snow, or light rain) may result in gaps in the final outputs or a lower visualisation quality^{45,46}. This occurs, for example, in 20250129_02_DEM_L2 due to the presence of snow, or in 20250130_08_DEM_L2 due to the presence of water. In terms of overlapping, all topographic products in this repository exhibit excellent quality in their central regions, although edge areas tend to show reduced quality due to fewer overlapping image captures.

During the creation of all orthomosaics using Pix4D photogrammetric processing, the average reprojection error – reflecting the deviation between each 3D point in the point cloud and its corresponding projection onto the 2D image plane – remained below 0.187 pixels. Consequently, this can be considered a highly precise value, as it is well below the threshold of 1 pixel, which is regarded as an accurate mean reprojection error. In addition, to ensure the quality of the final products, a visual inspection was conducted on the point clouds obtained after LiDAR processing to remove any unexpected outliers associated with the presence of low-altitude fog, uniform surfaces such as snow, and water surfaces. The classification framework proposed by Vieira *et al.*⁴⁷ was used to evaluate quality, categorising the data into high-quality areas with dense, consistent point coverage; medium-quality areas showing occasional 3D inconsistencies; and low-quality zones with limited point density or resolution.

Product ID	Representative Location of Interest	OR	DEM	Point Cloud	Observations
20250203_01	Entrance Point	HQ	HQ	HQ	No unusual patterns are observed in the outputs
20250129_02	Neptune's Bellows	HQ	MQ	MQ	DEM & PC with small gap in the Chilean's Window due to snow
20250129_03	Whalers Bay	HQ	HQ	HQ	DEM with small gaps in water areas. Those small water gaps in the PC have been cleaned
20250129_04	Green Glacier	HQ	HQ	HQ	Small water gaps in the PC have been cleaned
20250204_05	Black Glacier	HQ	HQ	MQ	PC with small gaps due to snow, which have been cleaned
20250129_05bis	Black Glacier	HQ	HQ	HQ	PC with small gaps due to snow, which have been cleaned
20250129_06	Pendulum Cove	HQ	HQ	HQ	Small water gaps in the PC have been cleaned
20250129_07	1970's Craters	HQ	HQ	HQ	DEM with small gaps in water areas
20250130_08	Telefon Bay	HQ	HQ	HQ	DEM with small gaps in water areas. Some anomalous points associated with the fog have been cleaned in the PC
20250130_09	Murature	HQ	HQ	HQ	DEM with small gaps in water areas. Some anomalous black points caused by low overlap have been cleaned in the PC
20250130_10	Fumarole Bay	HQ	HQ	MQ	DEM with small gaps in water areas
20250203_11	Argentine Base Deception	MQ	HQ	MQ	Orthomosaic with small blurry areas due to fog. DEM & PC with small gaps in water areas. Not cleaned
20250129_12	BAE GdC	HQ	HQ	HQ	Some anomalous black points caused by low overlap have been cleaned in the PC
20250130_13	Colatina	HQ	MQ	HQ	DEM with abnormal rectangle in a small area

Table 3. Quality check and personal evaluation conducted by the authors of the topographic products available in the FosterCoast repository. Abbreviations: orthomosaic (OR), Digital Elevation Model (DEM), Point Cloud (PC), High Quality (HQ), Medium Quality (MQ), and Low Quality (LQ).

Quality assessment. The original raw data used for processing is available within the repository. However, as detailed in earlier sections, the resulting topographic products have been processed to the highest standards, making them fully suitable for immediate use in data visualization and post-processing applications. A summary of the authors' thorough quality evaluation of the processed outputs is presented in Table 3, based on the aforementioned classification framework proposed by Vieira *et al.*⁴⁶.

In addition, in order to enhance confidence in the dataset's quality and its suitability for scientific applications, vertical discrepancies and the overall accuracy of the data presented in FosterCoast have been evaluated against the 2-meter spatial resolution Reference Elevation Model of Antarctica (REMA)⁴⁷. An RMSE of 1.124 m and an R^2 of 0.99 in a linear fit between the points indicate an error that, in the absence of GCPs, is negligible and does not affect the usability of the dataset. The full accuracy assessment can be found in the Supplementary Information section.

Usage Notes

Software. Being aware of the existence of commercial software specifically designed for visualising and post-processing the products available in FosterCoast, the authors recommend the following open-source alternatives: QGIS (QGIS Development Team, Geographic Information System, Open Source Geospatial Foundation Project, v.3.40.4, <https://qgis.org>), or SAGA GIS (Conrad *et al.* 2015) v.9.7.2 (<https://saga-gis.sourceforge.io/en/index.html>) for visualising orthomosaics and DEMs; CloudCompare v.2.13.2 (<http://www.cloudcompare.org/>), or LAsTools (rapidlasso GmbH, <https://rapidlasso.de/>).

Dataset application. In addition to accurately providing the most up-to-date record, to the best of our knowledge, of the coastline morphology of Port Foster Bay on Deception Island, as well as offering a robust database for conducting various geomorphological, volcanological, and hydrological studies in the monitored areas, FosterCoast holds great potential by supporting several complementary applications: (i) flight planning and execution safety, as UAV operators can use the generated DEMs and orthomosaics as a reference in the absence of GPS signals, a common challenge in Antarctica; (ii) tourism safety, as this repository provides updated information on the safest landing areas for tourists, as well as evacuation routes in emergency situations (*i.e.* possible volcanic eruptions); (iii) wildlife monitoring, by enabling centimeter-resolution tracking of certain communities of sea lions, chinstrap penguins, and some unique bryophyte species; (iv) landform processes, since DEMs and point clouds can be used to perform spatial morphometric analysis for studying the evolution of the topography in a specific area; and (v) quantitative glacial terrain analyses, including calving volume calculation, paleo-glacial feature identification, and paraglacial slope monitoring, among others. For further applications, it is recommended to consult Pina & Vieira⁴⁸ and Li *et al.*⁴⁹ for reviews of progress, current applications, and future use cases of UAVs in Antarctic research.

Code availability

UAV-based data processing was performed by following the instructions provided in the user manual of both softwares, DJI Terra and Pix4D Mapper for LiDAR and optical RGB data, respectively. These instructions can be found at https://dl.djicdn.com/downloads/dji-terra/20240118/DJI_Terra_User_Manual_v4.0__EN.pdf and <https://support.pix4d.com/hc/en-us/sections/360003718992-Manual>, respectively. In addition, the processing templates are included in the repository, in a dedicated top-level folder named “Processing templates”.

Received: 2 April 2025; Accepted: 30 July 2025;

Published online: 05 August 2025

References

1. Tovar-Sánchez, A., Román, A., Roque-Atienza, D. & Navarro, G. Applications of unmanned aerial vehicles in Antarctic environmental research. *Sci. Rep.* **11**, 21717, <https://doi.org/10.1038/s41598-021-01228-z> (2021).
2. Meredith, M. *et al.* Polar regions. (ipcc Special Report on the Ocean and Cryosphere in a Changing Climate, 2019).
3. Greene, C. A., Gardner, A. S., Schlegel, N.-J. & Fraser, A. D. Antarctic calving loss rivals ice-shelf thinning. *Nature* **609**, 948–958, <https://doi.org/10.1038/s41586-022-05037-w> (2022).
4. Ponti, S. & Guglielmin, M. Shore Evidences of a High Antarctic Ocean Wave Event: Geomorphology, Event Reconstruction and Coast Dynamics through a Remote Sensing Approach. *Remote Sens.* **13**, 518, <https://doi.org/10.3390/rs13030518> (2021).
5. Miles, B. W. J. & Bingham, R. G. Progressive unanchoring of Antarctic ice shelves since 1973. *Nature* **626**, 785–793, <https://doi.org/10.1038/s41586-024-07049-0> (2024).
6. Smale, D. A. & Barnes, D. K. A. Likely responses of the Antarctic benthos to climate-related changes in physical disturbance during the 21st century, based primarily on evidence from the West Antarctic Peninsula region. *Ecography (Cop.)* **31**, 289–305, <https://doi.org/10.1111/j.0906-7590.2008.05456.x> (2008).
7. Ducklow, H. W. *et al.* West Antarctic Peninsula: An Ice-Dependent Coastal Marine Ecosystem in Transition. *Oceanography* **26**(3), 190–203, <https://doi.org/10.5670/oceanog.2013.62> (2013).
8. Overeem, I. *et al.* Sea ice loss enhances wave action at the Arctic coast. *Geophys. Res. Lett.* **38**, 1–6, <https://doi.org/10.1029/2011GL048681> (2011).
9. Miles, B. W. J., Stokes, C. R. & Jamieson, S. S. R. Pan-ice-sheet glacier terminus change in East Antarctica reveals sensitivity of Wilkes Land to sea-ice changes. *Sci. Adv.* **2**, e1501350, <https://doi.org/10.1126/sciadv.1501350> (2016).
10. Reid, P. A. & Massom, R. A. Change and variability in Antarctic coastal exposure, 1979–2020. *Nat. Commun.* **13**, 1164, <https://doi.org/10.1038/s41467-022-28676-z> (2022).
11. Smellie, J. L. Lithostratigraphy and volcanic evolution of Deception Island, South Shetland Islands. *Antarct. Sci.* **13**(2), 188–209, <https://doi.org/10.1017/S0954102001000281> (2001).
12. Baker, P. E., Roobol, M. J. & Davies, T. G. The Geology of the South Shetland Islands: Volcanic Evolution of Deception Island. *BAS. Sci. Rep.* 1–110 (1975).
13. Almendros, J., Carmona, E., Jiménez, V., Díaz-Moreno, A. & Lorenzo, F. Volcano-Tectonic activity at Deception Island Volcano following a Seismic Swarm in the Bransfield Rift (2014–2015). *Geophys. Res. Lett.* **45**(10), 4788–4798, <https://doi.org/10.1029/2018gl077490> (2018).
14. Berrocoso, M. *et al.* Caldera unrest detected with seawater temperature anomalies at Deception Island, Antarctic Peninsula. *Bull. Volcanol.* **80**(4), 41, <https://doi.org/10.1007/s00445018-1216-2> (2018).
15. Bartolini, S., Geyer, A., Martí, J., Pedrazzi, D. & Aguirre-Díaz, G. Volcanic Hazard on Deception Island (South Shetland Islands, Antarctica). *J. Volcanol. Geotherm. Res.* **285**, 150–168, <https://doi.org/10.1016/j.jvolgeores.2014.08.009> (2014).
16. Bender, N. A., Crosbie, K. & Lynch, H. J. Patterns of tourism in the Antarctic Peninsula region: a 20-year analysis. *Antarct. Sci.* **28**(3), 194–203, <https://doi.org/10.1017/S0954102016000031> (2016).
17. Duarte, B. *et al.* Marine microbial community taxonomic and functional indicators to volcanic and anthropogenic stressors in Deception Island, Antarctica. *Environ. Sustain. Indic.* **24**, 100511, <https://doi.org/10.1016/j.indic.2024.100511> (2024).
18. Smith, K. L., Baldwin, R. J., Kaufmann, R. S. & Sturz, A. Ecosystem Studies at Deception Island, Antarctica: An Overview. *Deep-Sea Res. II* **50**, 1595–1609, [https://doi.org/10.1016/S0967-0645\(03\)00081-X](https://doi.org/10.1016/S0967-0645(03)00081-X) (2003).
19. Torrecillas, C., Zarzuelo, C., de la Fuente, J., Jigena-Antelo, B. & Prates, G. Evaluation and Modelling of the Coastal Geomorphological Changes of Deception Island since the 1970 Eruption and Its Involvement in Research Activity. *Remote Sens.* **16**, 512, <https://doi.org/10.3390/rs16030512> (2024).
20. Almar, R. *et al.* A Global Analysis of Extreme Coastal Waters Levels with Implications for Potential Coastal Overtopping. *Nat. Commun.* **12**, 3775, <https://doi.org/10.1038/s41467-021-24008-9> (2021).
21. Vousdoukas, M. I. *et al.* Global Probabilistic Projections of Extreme Sea Levels Show Intensification of Coastal Flood Hazard. *Nat. Commun.* **9**, 2360, <https://doi.org/10.1038/s41467-018-04692-w> (2018).
22. Brecher, H. H. Institute of Polar Studies Photogrammetric Maps of a Volcanic Eruption Area, Deception Island, Antarctica. *Research Foundation and the Institute of Polar Studies, The Ohio State University: Columbus, OH, USA* (1975).
23. Smellie, J. L. *et al.* Geology and geomorphology of Deception Island. *BAS GEOMAP Series, Sheets 6-A and 6-B, British Antarctic Survey, Cambridge*, pp: 78 (2002).
24. Murray, H., Lucieer, A. & Williams, R. Texture-based classification of sub-Antarctic vegetation communities on Heard Island. *Int. J. Appl. Earth Obs. Geoinf.* **12**, 138–149, <https://doi.org/10.1016/j.jag.2010.01.006> (2010).
25. Pfeifer, C. *et al.* Using fixed-wing UAV for detecting and mapping the distribution and abundance of penguins on the South Shetlands Islands, Antarctica. *Drones* **3**, 39, <https://doi.org/10.3390/drones3020039> (2019).
26. Barker, P. E. The Cenozoic subduction history of the Pacific margin of the Antarctic Peninsula: ridge crest-trench interactions. *J. Geol. Soc.* **139**, 787–801 (1982).
27. Torrecillas, C., Berrocoso, M., Felpeto, A., Torrecillas, M. D. & Garcia, A. Reconstructing palaeo-volcanic geometries using a Geodynamic Regression Model (GRM): Application to Deception Island volcano (South Shetland Islands, Antarctica). *Geomorphology* **182**, 79–88, <https://doi.org/10.1016/j.geomorph.2012.10.032> (2013).
28. Angulo-Preckler, C. *et al.* Volcanism and rapid sedimentation affect the benthic communities of Deception Island, Antarctica. *Cont. Shelf Res.* **220**, 104404, <https://doi.org/10.1016/j.csr.2021.104404> (2021).
29. Muñoz, P. A., Flores, P. A., Boehmwald, F. A. & Blamey, J. M. Thermophilic bacteria present in a sample from Fumarole Bay, Deception Island. *Antarct. Sci.* **24**(6), 549–555, <https://doi.org/10.1017/S0954102011000393> (2011).
30. Turner, D., Lucieer, A. & Watson, C. An Automated Technique for Generating Georectified Mosaics from Ultra-High Resolution Unmanned Aerial Vehicle (UAV) Imagery, Based on Structure from Motion (SfM) Point Clouds. *Remote Sens.* **4**(5), 1392–1410, <https://doi.org/10.3390/rs4051392> (2012).
31. SCAR. State of knowledge of wildlife responses to remotely piloted aircraft systems (RPAS). **11**, <https://www.scar.org/antarctic-treaty/actm-papers/atcm-xl-and-cep-xx-2017-beijing-china/2974-atcm40-wp020/> (2017).
32. Hodgson, J. C. & Koh, L. P. Best practice for minimising unmanned aerial vehicle disturbance to wildlife in biological field research. *Curr. Biol.* **26**, R404–R405, <https://doi.org/10.1016/j.cub.2016.04.001> (2016).

33. GNSS Service Spanish Geographic Institute [IGN]. Index of /ERGNSS. <https://datos-geodesia.ign.es/ERGNSS/> (2025)
34. Román, A. *et al.* ShetlandsUAVmetry: unmanned aerial vehicle-based photogrammetric dataset for Antarctic environmental research. *Sci. Data* **11**, 202, <https://doi.org/10.1038/s41597-024-03045-1> (2024).
35. Westoby, M. J., Brasington, J., Glasser, N. F., Hambrey, M. J. & Reynolds, J. M. “Structure-from-Motion” photogrammetry: A low cost, affective tool for geoscience applications. *Geomorphology* **179**, 300–314, <https://doi.org/10.1016/j.geomorph.2012.08.021> (2012).
36. Smith, M. W., Carrivick, J. L. & Quincey, D. J. Structure from motion photogrammetry in physical geography. *Prog. Phys. Geog.* **40**, 247–275, <https://doi.org/10.1016/j.geomorph.2012.08.021> (2016).
37. Dering, G. M., Mickethwaite, S., Thiele, S. T., Vollgger, S. A. & Cruden, A. R. Review of drones, photogrammetry and emerging sensor technology for the study of dykes: Best practices and future potential. *J. Volcanol. Geoth. Res.* **373**, 148–166, <https://doi.org/10.1016/j.jvolgeores.2019.01.018> (2019).
38. Román, A. *et al.* LiDAR-based topographic data for the coastline of Port Foster, Deception Island. *figshare* <https://doi.org/10.6084/m9.figshare.28696421> (2025).
39. Tomaščík, J., Mokroš, M., Surový, P., Grznárová, A. & Merganič, J. UAV RTK/PPK Method—An Optimal Solution for Mapping Inaccessible Forested Areas? *Remote Sens.* **11**(6), 721, <https://doi.org/10.3390/rs11060721> (2019).
40. Štroner, M., Urban, R., Reindl, T., Seidl, J. & Brouček, J. Evaluation of the Georeferencing Accuracy of a Photogrammetric Model Using a Quadcopter with Onboard GNSS RTK. *Sensors* **20**(8), 2318, <https://doi.org/10.3390/s20082318> (2020).
41. Štroner, M., Urban, R., Reindl, T., Seidl, J. & Brouček, J. Photogrammetry Using UAV-Mounted GNSS RTK: Georeferencing Strategies without GCPs. *Remote Sens.* **13**(7), 1336, <https://doi.org/10.3390/rs13071336> (2021).
42. Zhang, H. *et al.* Evaluating the potential of post-processing kinematic (PPK) georeferencing for UAV-based structure- from-motion (SfM) photogrammetry and surface change detection. *ESurf* **7**, 807–827, <https://doi.org/10.5194/esurf-7-807-2019> (2019).
43. Dandois, J. P., Olano, M. & Ellis, E. C. Optimal Altitude, Overlap, and Weather Conditions for Computer Vision UAV Estimates of Forest Structure. *Remote Sens.* **7**(10), 13895–13920, <https://doi.org/10.3390/rs71013895> (2015).
44. Torres-Sánchez, J., López-Granados, F., Borra-Serrano, I. & Peña, J. M. Assessing UAV-collected image overlap influence on computation time and digital surface model accuracy in olive orchards. *Precision Agric.* **19**, 115–133, <https://doi.org/10.1007/s11119-017-9502-0> (2018).
45. Elhadary, A., Rabah, M., Ghanim, E., Mohie, R. & Taha, A. The influence of flight height and overlap on UAV imagery over featureless surfaces and constructing formulas predicting geometrical accuracy. *NRIAG J. Astron. Geophys.* **11**(1), 210–223, <https://doi.org/10.1080/20909977.2022.2057148> (2023).
46. Vieira, G., Mora, C., Pina, P., Ramalho, R. & Fernandes, R. UAV-based very high resolution point cloud, digital surface model and orthomosaic of the Chãdas Caldeiras lava fields (Fogo, Cabo Verde). *Earth Syst. Sci. Data* **13**, 3179–3201, <https://doi.org/10.5194/essd-13-3179-2021> (2021).
47. Howat, I. *et al.* The Reference Elevation Model of Antarctica – Mosaics, Version 2. *Harvard Dataverse*, **1**, <https://doi.org/10.7910/DVN/EBW8UC> (2022).
48. Pina, P. & Vieira, G. UAVs for Science in Antarctica. *Remote Sens.* **14**, 1610, <https://doi.org/10.3390/rs14071610> (2022).
49. Li, Y., *et al.* Unmanned Aerial Vehicle Remote Sensing for Antarctic Research. *IEEE Geosci. Remote Sens. Mag.* 73–93, <https://doi.org/10.1109/MGRS.2022.3227056> (2023).
50. Matsuoka, K. *et al.* Quantarctica, an integrated mapping environment for Antarctica, the Southern Ocean, and sub-Antarctic islands. *Environ. Model. Softw.* **140**, 105015, <https://doi.org/10.1016/j.envsoft.2021.105015> (2021).

Acknowledgements

This research was funded by the Spanish Government project PID2021-1257830B-I00 (DICHOSO). Sensors and UAV were funded by Spanish Government Infrastructure CSIC EQC2018-004275-P and EQC2019-005721. A. Román, staff hired under the Generation D initiative, promoted by Red.es, an organisation attached to the Ministry for Digital Transformation and the Civil Service, for the attraction and retention of talent through grants and training contracts, financed by the Recovery, Transformation and Resilience Plan through the European Union's Next Generation funds. The authors warmly thank crew of the BIO Hespérides and the B/O Sarmiento de Gamboa, the military staff of the Spanish Antarctic Base Gabriel de Castilla and the Marine Technology Unit (UTM-CSIC) for their logistic support, without which the XXXVIII Spanish Antarctic campaign and this work would not have been possible. We also thank Amós de Gil and Carlos Garcia from University of Cádiz (UCA), and Rafael Abella and Anselmo García from the Spanish Geographic Institute (IGN), for their invaluable support during the Antarctic campaign in relation to the operation of the equipment and the acquisition of accurate GPS positioning data, respectively. This work represents a contribution to Polar CSIC-HUBs.

Author contributions

A.T.-S., M.L., G.N. and A.R. designed the structure of the research; A.T.-S., G.N. and A.R. participated in the Antarctic campaign, collecting data by flying the UAVs; M.L., F.A. and A.R. performed aerial data processing by using commercial processing software and prepared the data for publication in a repository; A.R. wrote the first draft of the manuscript, which was reviewed and edited by A.T.-S., M.L., F.A. and G.N.

Competing interests

The authors declare that they have no known competing financial interests or personal relationships that could have appeared to influence the research reported in this paper.

Additional information

Supplementary information The online version contains supplementary material available at <https://doi.org/10.1038/s41597-025-05726-x>.

Correspondence and requests for materials should be addressed to A.R.

Reprints and permissions information is available at www.nature.com/reprints.

Publisher's note Springer Nature remains neutral with regard to jurisdictional claims in published maps and institutional affiliations.



Open Access This article is licensed under a Creative Commons Attribution-NonCommercial-NoDerivatives 4.0 International License, which permits any non-commercial use, sharing, distribution and reproduction in any medium or format, as long as you give appropriate credit to the original author(s) and the source, provide a link to the Creative Commons licence, and indicate if you modified the licensed material. You do not have permission under this licence to share adapted material derived from this article or parts of it. The images or other third party material in this article are included in the article's Creative Commons licence, unless indicated otherwise in a credit line to the material. If material is not included in the article's Creative Commons licence and your intended use is not permitted by statutory regulation or exceeds the permitted use, you will need to obtain permission directly from the copyright holder. To view a copy of this licence, visit <http://creativecommons.org/licenses/by-nc-nd/4.0/>.

© The Author(s) 2025